Space Weather

RESEARCH ARTICLE
10.1029/2024SW004084

Interhemispheric Asymmetry in the High-Latitude Neutral Density Variations During the 13–14 March 2022 Storm

Qingyu Zhu[1], **Gang Lu**[2], **Sarah Vines**[3], **and Marc Hairston**[1]

[1]William B Hanson Center for Space Sciences, University of Texas at Dallas, Richardson, TX, USA, [2]High Altitude Observatory, National Center for Atmospheric Research, Boulder, CO, USA, [3]Space Science Division, Southwest Research Institute, San Antonio, TX, USA

Key Points:

- GITM precisely models high-latitude neutral density anomalies (HDAs) in the second recovery phase of the 13–14 March 2022 storm
- HDAs in the different hemispheres exhibit differences in magnitudes, propagation speeds, and propagation directions
- Interhemispheric asymmetries (IHAs) in HDA's magnitude and propagation stem from IHAs in Joule heating and background thermospheric condition

Supporting Information:

Supporting Information may be found in the online version of this article.

Correspondence to:

Q. Zhu,
qingyu.zhu@utdallas.edu

Citation:

Zhu, Q., Lu, G., Vines, S., & Hairston, M. (2024). Interhemispheric asymmetry in the high-latitude neutral density variations during the 13–14 March 2022 storm. *Space Weather*, *22*, e2024SW004084. https://doi.org/10.1029/2024SW004084

Received 23 JUL 2024
Accepted 29 OCT 2024

Abstract During the second recovery phase of the 13–14 March 2022 storm, intense high-latitude neutral mass density spikes are detected by satellites at ~500 km in both hemispheres. These density spikes, accurately modeled by the Global Ionospheric Thermosphere Model (GITM), are identified as high-latitude neutral mass density anomalies (HDAs). The GITM simulation indicates that these HDAs, which extends over the polar region, are important features in high-latitude neutral density. Furthermore, GITM reveals that these HDAs are manifestations of transpolar traveling atmospheric disturbances triggered on the dawn side. Moreover, GITM also reveals significant interhemispheric asymmetries (IHAs) in the magnitude, propagation speed, and propagation direction of HDAs, which are linked to the IHAs in the distribution and magnitude of Joule heating deposited as well as the thermospheric background conditions. This study presents a dynamic perspective on the IHA of storm-time high-latitude neutral density variations that is particularly helpful to the proper interpretation of satellite observations.

Plain Language Summary During intense geomagnetic storms, thermospheric neutral mass density increases significantly due to the drastic increase in energy inputs from the magnetosphere. The enhanced neutral mass density can increases drag on low Earth orbit satellites, complicating their orbit predictions and increasing the risk of collisions with other space objects. Particularly in the polar regions, satellites often detect sharp spikes in neutral mass density. These density spikes are associated with the neutral density structures, which are termed as high-latitude neutral density anomalies (HDAs), Understanding how these HDAs form and evolve is crucial for predicting changes in neutral density in the polar regions during storms, yet our knowledge of these phenomena, especially their differences between the northern and southern hemispheres, is still very limited. This study aims to examine these interhemispheric differences in the evolution of HDAs during a geomagnetic storm and explore the underlying causes driving these asymmetries. This study provides new insights into the interhemispheric differences in the high-latitude neutral mass density variations.

1. Introduction

During geomagnetic storms, substantial electromagnetic energy is deposited in the Earth's thermosphere, primarily in the form of Joule heating, which significantly enhances thermospheric neutral mass density (Prölss, 2011; Richmond, 2021). Enhanced thermospheric neutral density during geomagnetic storms increases drag on low Earth orbit satellites, potentially lowering their orbits and causing reentry. Variations in thermospheric neutral density complicates orbit predictions and heightens collision risks with other space objects (Oliveira & Zesta, 2019). Hence, understanding these density changes is crucial for precise satellite orbit determination and effective collision avoidance.

Storm-time neutral mass density variations display significant interhemispheric asymmetries (IHAs), especially at low and middle latitudes, as evidenced by satellite measurement studies (Aa et al., 2012; Bruinsma et al., 2006; R. Li & Lei, 2021; Sutton et al., 2005; Zhu et al., 2023). IHAs at high latitudes, however, have received less focus. Yamazaki et al. (2015) demonstrated that there are notably IHAs in high-latitude neutral mass density variations when the y-component of the interplanetary magnetic field (IMF B_y) is strong, a finding confirmed by simulations from Hong et al. (2021). Nonetheless, these studies primarily viewed the IHAs in the high-latitude neutral density statically, neglecting the dynamics in high-latitude neutral density variations. As noted by Balthazor and Moffett (1999) and Lu et al. (2016), intense Joule heating deposited in the auroral zone can trigger transpolar traveling atmospheric disturbances (TADs). These TADs can lead to neutral density enhancement over the polar region,

observable by satellites as intense neutral density spikes (Huang et al., 2017; Liu et al., 2010; Lu et al., 2016). In this paper, these elongated neutral density enhancements are termed high-latitude neutral density anomalies (HDAs). The peak of these HDAs can be 100% higher than the surrounding ambient neutral density, significantly increasing air drag across a large area at high latitudes. Additionally, the HDAs can propagate with a phase speed more than 600 m/s (Bruinsma & Forbes, 2009; Lu et al., 2016). Given the dynamic nature and the critical importance of HDAs, it is crucial to understand the IHAs in the HDAs to further our knowledge of the IHA in the storm-time variations of high-latitude neutral densities, an area where current understanding is still limited.

In this study, we aim to unveil the IHA in the HDA during a focused event study. We will focus on a moderate to intense geomagnetic storm that occurred on 13–14 March 2022, noted for its significant geo-effective impacts (Aa et al., 2023). Intense HDAs have been detected by low-Earth-orbit satellites in both hemispheres during the second recovery phase of this storm, and we will utilize the Global Ionosphere Thermosphere Model (GITM, Ridley et al., 2006) to analyze their formation and evolution of the HDAs across the different hemispheres. To improve the high-latitude forcing specification in GITM, we will incorporate the field-aligned currents (FACs) from the Active Magnetosphere and Planetary Electrodynamics Response Experiment (AMPERE, Anderson et al., 2021). Our goal is to elucidate the IHAs in the formation and evolution of HDAs and to identify the underlying causes driving these asymmetries.

2. Methodology

2.1. Data

2.1.1. Neutral Mass Density Measurements

Neutral mass density measurements from the Gravity Recovery and Climate Experiment Follow-On (GRACE-FO) and Swarm-C satellites are utilized to investigate the high-latitude neutral mass density variations. Both satellites fly in near-circular polar orbits with an orbital period of approximately 96 min. During the 13–14 March 2022 storm, GRACE-FO orbits between 480 and 530 km with an ascending node at 16 solar local time (SLT), while Swarm-C orbits between 430 and 460 km with an ascending node at 6 SLT. The neutral mass density data from GRACE-FO and Swarm-C are derived from high-precision accelerometer measurements of non-gravitational forces. The GRACE-FO and Swarm-C data have a temporal resolution of 10 s, corresponding to a spatial resolution of approximately 75 km. The level-2 Swarm-C neutral density data is used in this study. Details regarding the accelerometer density data can be found in the works of Hładczuk et al. (2024) and references therein.

2.1.2. AMPERE FAC

The AMPERE FAC patterns utilized in this study are derived from the magnetic field perturbation measurements collected by 66 Iridium NEXT satellites. Each satellite operates in a near-polar orbit at an orbital altitude of 780 km, with an orbital period of 104 min. These 66 Iridium satellites are distributed along 6 orbital planes spaced in the geographic longitude by 30°. Each Iridium satellite carries a vector fluxgate magnetometer that is able to sample the vector magnetic field. Following the processing of raw magnetic perturbation data, fitting with spherical cap harmonic basis functions is applied to data within a 10-min time window, aiming to derive a global distribution of magnetic perturbations at high latitudes. The intrinsic spatial resolution of the fitted magnetic perturbation distribution is 3° in Magnetic Latitude (MLAT) and 2.4 hr in Magnetic Local Time (MLT). From these, FACs are computed using the curl of the fitted horizontal magnetic perturbations. The spatial resolution of the fitted FAC patterns is 1 hr in MLT and 1° in MLAT. More details regarding the AMPERE FAC can be found in Anderson et al. (2021) and Waters et al. (2020). In this study, the 2-min resolution AMPERE FAC data are used and smoothed in both MLT and MLAT directions with a weighted sliding window to filter out mesoscale FAC structures prior to their integration into GITM. The filtering is applied because some mesoscale FAC structures may result from numerical artifacts. Details on the smoothing process and the integration of AMPERE FAC data into the GITM can be found in Zhu et al. (2022).

2.1.3. ICON-MIGHTI Meridional Winds

In this study, the F-region meridional wind measurements provided by the Ionospheric Connection Explorer's Michelson Interferometer for Global High-resolution Thermospheric Imaging instrument (ICON-MIGHTI,

Englert et al., 2017; Immel et al., 2018) are used to assess the effectiveness of GITM in capturing F-region neutral dynamics. ICON orbits at an altitude of 575 km with an inclination angle of 27°. MIGHTI measures the horizontal winds in the F-region by observing the line-of-sight Doppler shift of the atomic oxygen emission line at 630 nm from Earth's limb (Englert et al., 2023; Harding et al., 2017; Makela et al., 2021). For our analysis, we utilized the version-5 meridional wind data, which has a temporal resolution of 60 s on the day side and 30 s on the nightside (Harding et al., 2024; Li et al., 2024).

2.2. GITM

GITM is a three-dimensional general circulation model designed for the Earth's upper atmosphere (Ridley et al., 2006). It self-consistently solves for the density, velocity, and temperature of neutrals, ions, and electrons. GITM offers flexible grid size options and relaxes the hydrostatic assumption to permit the propagation of acoustic waves (Deng et al., 2021; Tyska et al., 2024). In this study, GITM is coupled with the 3Dynamo solver (Maute & Richmond, 2017) to calculate the global electric field using the AMPERE FAC inputs, and details about the coupling can be found in Zhu et al. (2022). For the simulation carried out in this study, GITM is configured with a spatial resolution is set at 5° in geographic longitude, 2.5° in geographic latitude, and 1/3 scale height in altitude. The model runs with a time step of 2 s. Additionally, the 3Dynamo solver has its reference height set at 110 km, with a uniform MLT resolution of 0.24 hr. The 3Dynamo solver grid consists of 161 points in MLAT, providing a spatial resolution of 2–3° in the auroral zone and less than 0.5° near the geomagnetic equator.

In this study, auroral electron precipitation in GITM is specified by using a recently developed empirical model called Auroral Spectra and High-Latitude Electric field variabilitY (ASHLEY, Zhu et al., 2021), specifically its electron precipitation module, ASHLEY-A. ASHLEY-A provides statistical distributions of differential energy flux ranging from 30 eV to 30 keV without presuming a specific type of energy spectrum (e.g., a Maxwellian spectrum) for various interplanetary magnetic field (IMF) and solar wind conditions. This significantly improves the specification of soft (<1 keV) electron precipitations, thereby significantly enhancing the thermospheric neutral mass density estimation above 400 km (Zhu, Deng, et al., 2022). Hence, ASHLEY-A is used to specify the electron precipitation in GITM in this study.

Figure 1 displays the electric potential, electron precipitation, and Joule heating outputs for the NH and SH at 18:30 UT on 03/13/2022. At high latitudes, both positive and negative electric potential cells are visible. In the NH, the positive cell is round with a greater magnitude than the negative cell. In the SH, the positive cell has a crescent shape and a weaker magnitude, consistent with patterns observed when the IMF has a negative B_y component (Zhu et al., 2021). The IMF variations will be discussed in the next section. The second panel illustrates the total energy flux of electron precipitation. As noted by Zhu et al. (2021), >1 keV electron precipitation, which largely determines the total energy flux, does not exhibit a strong statistical dependence on the IMF B_y. Since these >1 keV electron precipitation also significantly contributes to the high-latitude ionospheric conductance, the high-latitude ionospheric conductance between the different hemispheres remains unaffected by the IMF B_y in the GITM simulation due to the implementation of ASHLEY-A. The IMF B_y influence on the electric potential shown in the first panel primarily arises from the FACs. The third panel shows the height-integrated Joule heating, which is primarily concentrated on the dawn side and is stronger in the NH at this UT. The stronger Joule heating in the NH may result from stronger dawn-side electric fields (evidenced by denser equipotential contours) and higher ionospheric conductance (heating occurring on the day side).

3. Results and Discussion

Figure 2a illustrates temporal variations of the IMF during this event. The IMF B_y predominantly remains negative on March 13, while the IMF B_z exhibits three distinct southward excursions, each lasting 2–3 hr. Concurrent with these southward excursions, the SYM-H index experiences three pronounced decreases (Figure 2b), indicating that the storm has three main phases. The SYM-H index reaches a minimum value of −120 nT at the end of March 13. Meanwhile, as depicted in Figure 2c, the total FAC (hemispheric integral of the AMPERE FAC magnitude) in each hemisphere also shows significant enhancements corresponding to each southward excursion of the IMF B_z, with peaks reaching 20 MA. The total FACs are generally comparable across both hemispheres. Figure 2d displays the cross-polar-cap potential (CPCP) computed in the GITM in the different hemispheres. Generally, CPCP is comparable between the NH and SH, and it peaks at around 200 kV during the main phases. However, between 11 and 12 UT on March 13, CPCP surges to 400 kV, which may be an

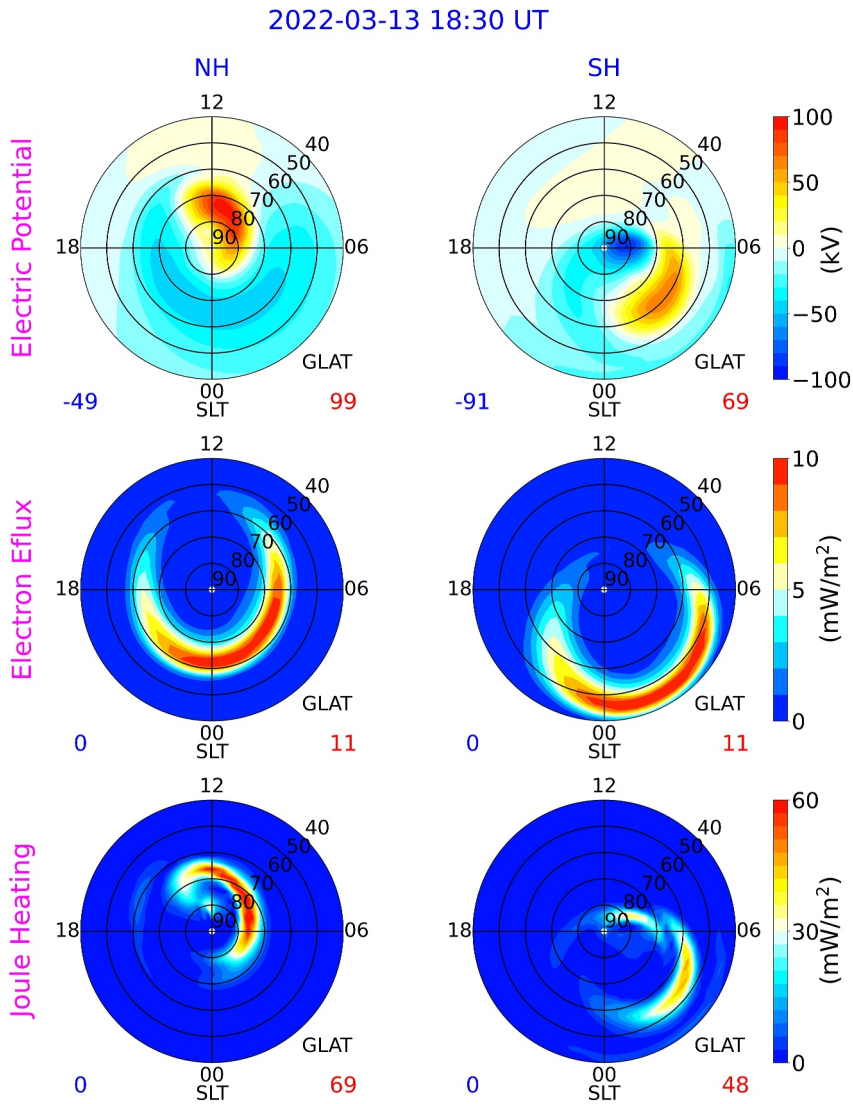

Figure 1. Distributions of the (top) electric potential (middle) total electron energy flux and (bottom) height-integrated Joule heating from the FAC-driven GITM simulation in the (left) NH and (right) SH at 18:30 UT on 03/13/2022. The minimum and maximum of the parameter are labeled at the bottom left and right of each plot, respectively. All plots are present in geographic coordinates.

overestimation. This is supported by a comparison with Figures 2d and 2f, where despite substantial FAC enhancements from 10 to 12 UT, the hemispheric auroral power (HP) remains relatively low, suggesting potential inconsistencies between FAC and electron precipitation in GITM. Here, HP is the hemispheric integral of the total electron energy flux provided by ASHLEY-A. Figure 3 and supplementary Figures S1 in Supporting Information S1 provide a comparison between the observed and simulated horizontal cross-track ion drifts along Defense Meteorological Satellite Program (DMSP) satellites in the NH and SH from 11 UT on March 13. Notably, a significant overestimation of ion drift is observed between 11:10 and 12:30 UT which suggests that the CPCP is overestimated during this period. Outside this period, the data-model comparisons generally align well, affirming that the FAC-driven GITM simulation effectively captures high-latitude electric fields during most time of this event. Figure 2e depicted the total Joule heating from GITM in both hemispheres. Despite the absence of significant IHA in the CPCP, the total Joule heating exhibits notable differences between the two hemispheres. Specifically, around 18 UT on March 13, Joule heating in the NH peaks at approximately 600 GW, which is about 50% higher than that in the SH.

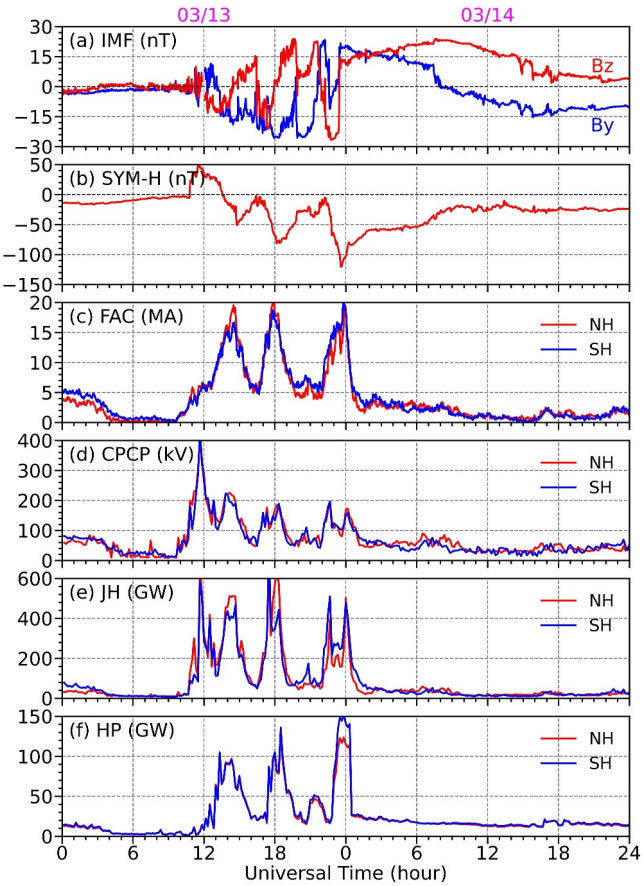

Figure 2. Temporal evolutions of (a) interplanetary magnetic field B_y (blue) and B_z (red) components, (b) SMR index, (c) hemispheric integrated field-aligned currents, (d) cross-polar-cap potential, (e) hemispheric integrated Joule heating and (f) hemispheric integrated auroral power during 13–14 March 2022. For panels c–f, red and blue lines represent the Northern and Southern Hemispheres, respectively. The hemispheric integrated field-aligned current is calculated using the AMPERE FAC. The hemispheric integrated auroral power is the hemispheric integral of the total electron energy flux provided by ASHLEY.

Figures 4a and 4b display the comparisons of observed and simulated neutral mass density along the trajectories of the GRACE-FO and Swarm-C satellites, respectively. For each UT, the neutral mass density outputs from GITM are interpolated spatiotemporally along the satellite trajectory. Overall, the FAC-driven GITM simulation (red line) adequately captures the observed variations in neutral mass density (black line) during the geomagnetic storm on March 13, although there are some quantitative discrepancies between data and model results. Notably, the FAC-driven GITM simulation accurately captures the most pronounced high-latitude spikes in the neutral mass density observed by both GRACE-FO and Swarm-C around 18:50 UT (marked by vertical magenta dashed lines). However, the magnitude of these spikes is underestimated. The underestimation may be partly due to an underestimation of Joule heating and partly due to GITM's general tendency to underestimate the quiet-time neutral density baseline (e.g., before 11 UT). The underlying cause of this baseline discrepancy deserves further investigation. The FAC-driven GITM simulation also successfully captures several high-latitude neutral density spikes in the SH, both before and after 18:50 UT.

The green line in Figures 4a and 4b represents the GITM simulation results when both the high-latitude electron precipitation and electric field are specified by empirical models. The empirical model used for the high-latitude electric field is ASHLEY-E, which is the electric potential component of ASHLEY and provides climatological electric potential patterns based on given IMF and solar wind conditions (Zhu et al., 2021). This simulation will be referred to as the ASHLEY-driven GITM simulation. It is evident that the ASHLEY-driven GITM simulation does not adequately reproduce thermospheric density variations, particularly failing to capture the location and magnitude of the observed neutral density spikes around 18:50 UT. The poorer data-model comparison is likely due to that ASHLEY-E is unable to represent the high-latitude electric field as accurate as the FAC-driven simulation, resulting in larger uncertainties in the estimation of Joule heating. While some discrepancies remain between the FAC-driven GITM simulation and the observations, the FAC-driven results are generally satisfactory for this event. Hence, the FAC-driven simulation with ASHLEY-A is used for further analysis. In the remainder of this manuscript, we will primarily focus on high-latitude thermospheric density variations during the second main and recovery phases of the storm, as the most pronounced high-latitude density spikes occur during this period. While high-latitude density spikes are also observed during the first and third main and recovery phases, they are much less intense.

Figure 5 compare the measured and simulated neutral mass density from three consecutive polar crossings of GRACE-FO and Swarm-C between 17:45 and 19:50 UT. Figure 5b highlights the most pronounced neutral density spikes (labeled as Spike 1), identified around 18:50 UT. The spikes shown in Figure 5b peak around 80° magnetic latitude (MLAT) and exhibit densities that are around 100% higher than the surrounding ambient levels. The full width at half maximum (FWHM) of the spikes is approximately 2,000 km. While the GITM underestimates their magnitudes, it accurately locates these spikes over the polar regions. Following the identification of Spike 1, a high-latitude density spike is also observed in the SH (labeled as Spike 2) between 19:30 and 19:40 UT, which is also well captured by GITM. As shown in Figure 5c, Spike 2 has a full width at half maximum (FWHM) of approximately 2,200 km and peaks around −75° MLAT. As will be discussed later, Spikes 1 and 2 correspond to HDAs formed prior to their detection by the satellites in the NH and SH, respectively. In addition to Spikes 1 and 2, several neutral density spikes with smaller FWHM values are identified at high latitudes (e.g., black arrows in Figures 5a and 5c). These smaller-scale neutral density spikes might result from Joule heating associated with mesoscale high-latitude forcings (Sheng et al., 2022), which are not included in GITM for this study. As discussed in Section 2, only large-scale FAC is incorporated into GITM, and ASHLEY-A provides

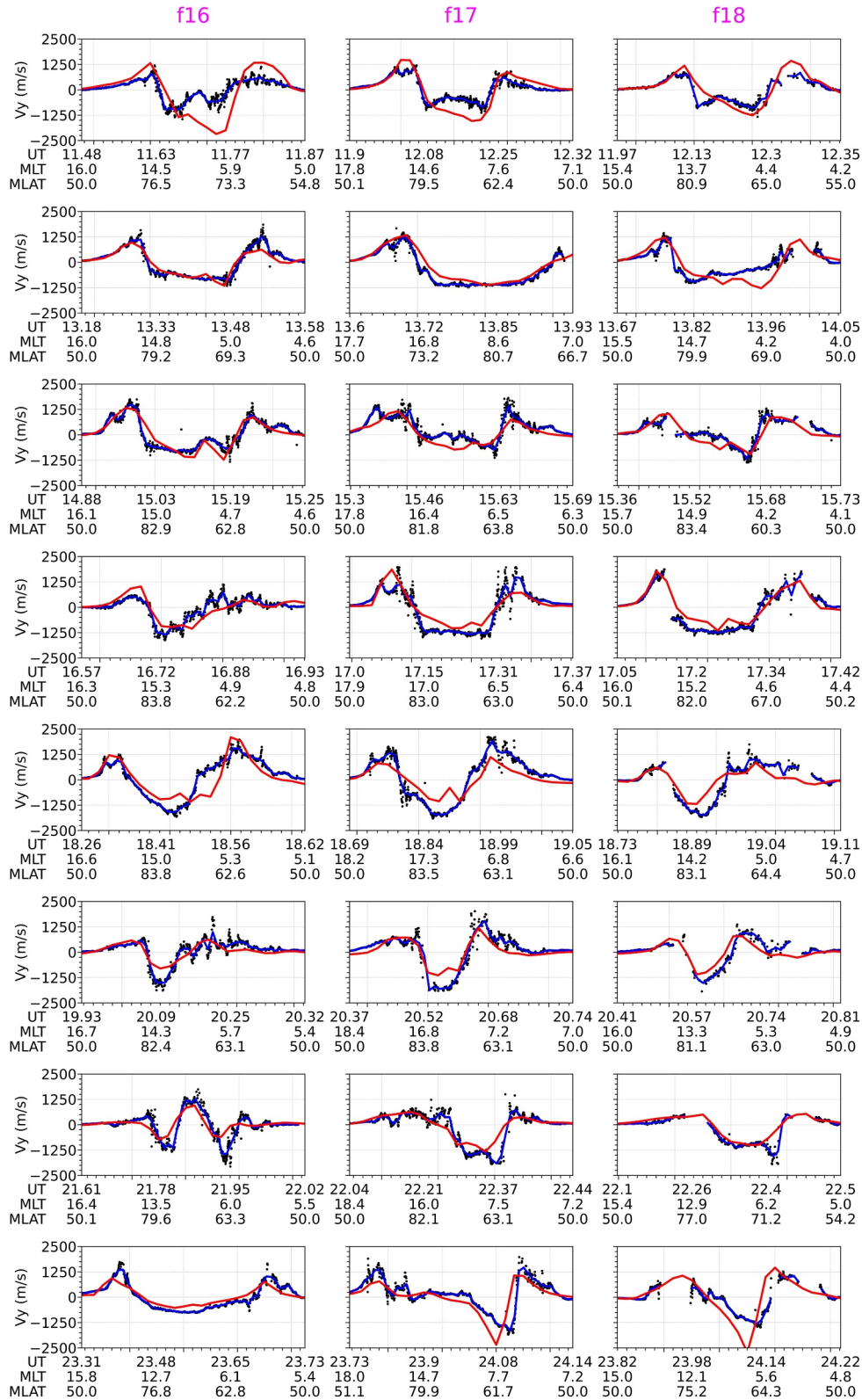

Figure 3. Comparisons of the cross-track ion drifts along the Defense Meteorological Satellite Program (DMSP) polar crossings in the Northern Hemisphere. In each plot, the black dots represent the unsmoothed DMSP cross-track ion drift, the blue line indicates the smoothed DMSP cross-track ion drift using a 500-km sliding window, and the red line represents the cross-track ion drift from the FAC-driven simulation.

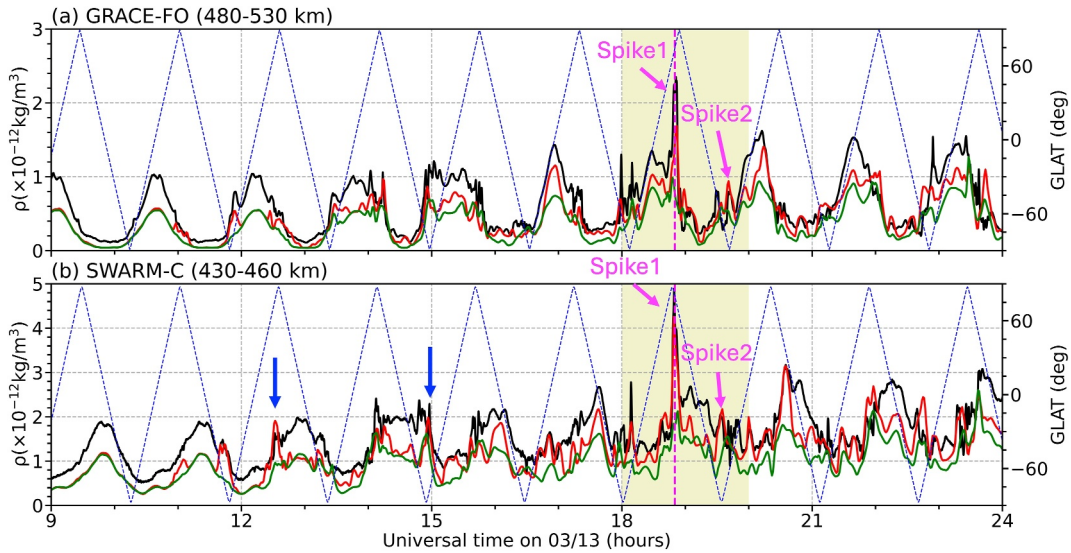

Figure 4. Comparisons between observed and simulated thermospheric neutral mass density data for the (a) GRACE-FO and (b) Swarm-C satellites on 03/13. Observational data are depicted with black lines, FAC-driven GITM outputs are represented in red lines and ASHLEY-driven GITM outputs are shown in green lines. The geographic latitude of each satellite is indicated by blue dashed lines. The vertical dashed line in panels a and b highlights the universal time of the most significant neutral density spike detected by the satellites. Spikes 1 and 2 correspond to those in Figure 5.

large-scale electron precipitation. As a result, mesoscale high-latitude forcings are not included in GITM, which may lead to poor representations of these spikes with smaller scale sizes.

Figure 6 displays the neutral mass density at 500 km and height-integrated Joule heating in both the NH and SH between 18 and 20 UT on March 13. The trajectories of GRACE-FO and Swarm-C satellites are overlaid on the plots of neutral mass density (i.e., first and third rows). Notably, there is significant Joule heating deposited on the dawn side in both hemispheres before 18:30 UT. In the NH, Joule heating is primarily concentrated in the dawn to noon sector, whereas in the SH, it is predominantly deposited from post-midnight to dawn. Additionally, Joule

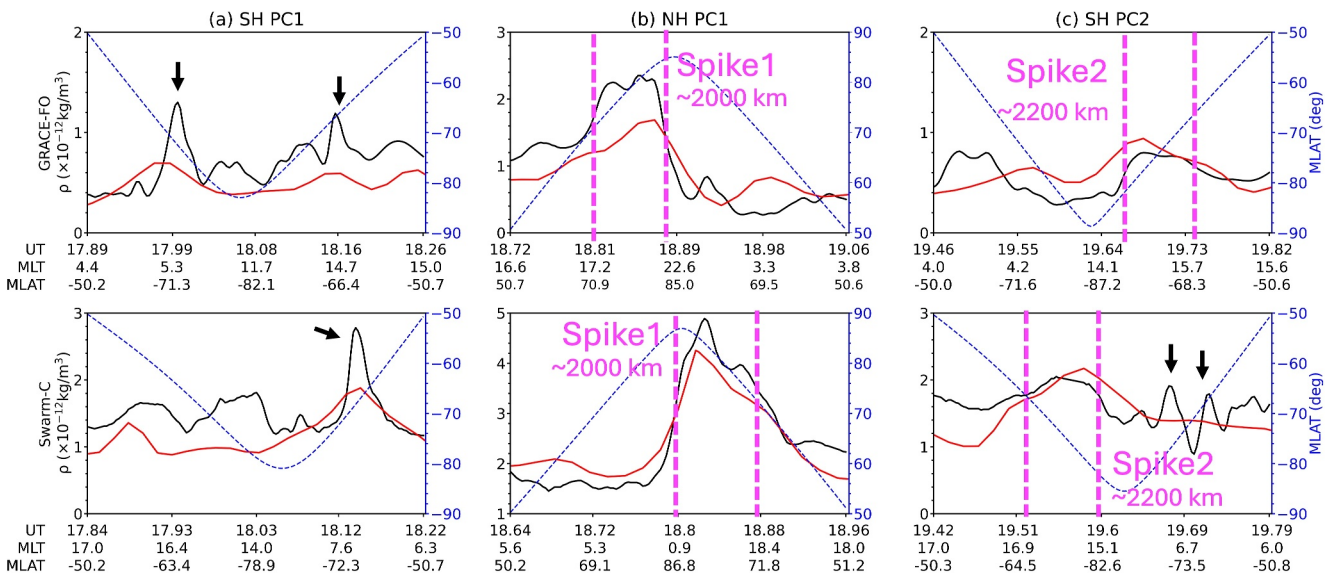

Figure 5. Three polar crossings by GRACE-FO and Swarm-C between 17:45 and 19:50 UT. In these plots, actual measurements of neutral mass density are shown with black lines, and simulations are in red. The magnetic latitude of the satellite's path is marked by a blue dashed line in each plot. In panels b and c, the magenta lines denote the half-maximum level of the spike, and the corresponding full width at half maximum (FWHM) of the spike is labeled. Black arrows in panels a and c marked some density spikes with smaller FWHM values.

10.1029/2024SW004084

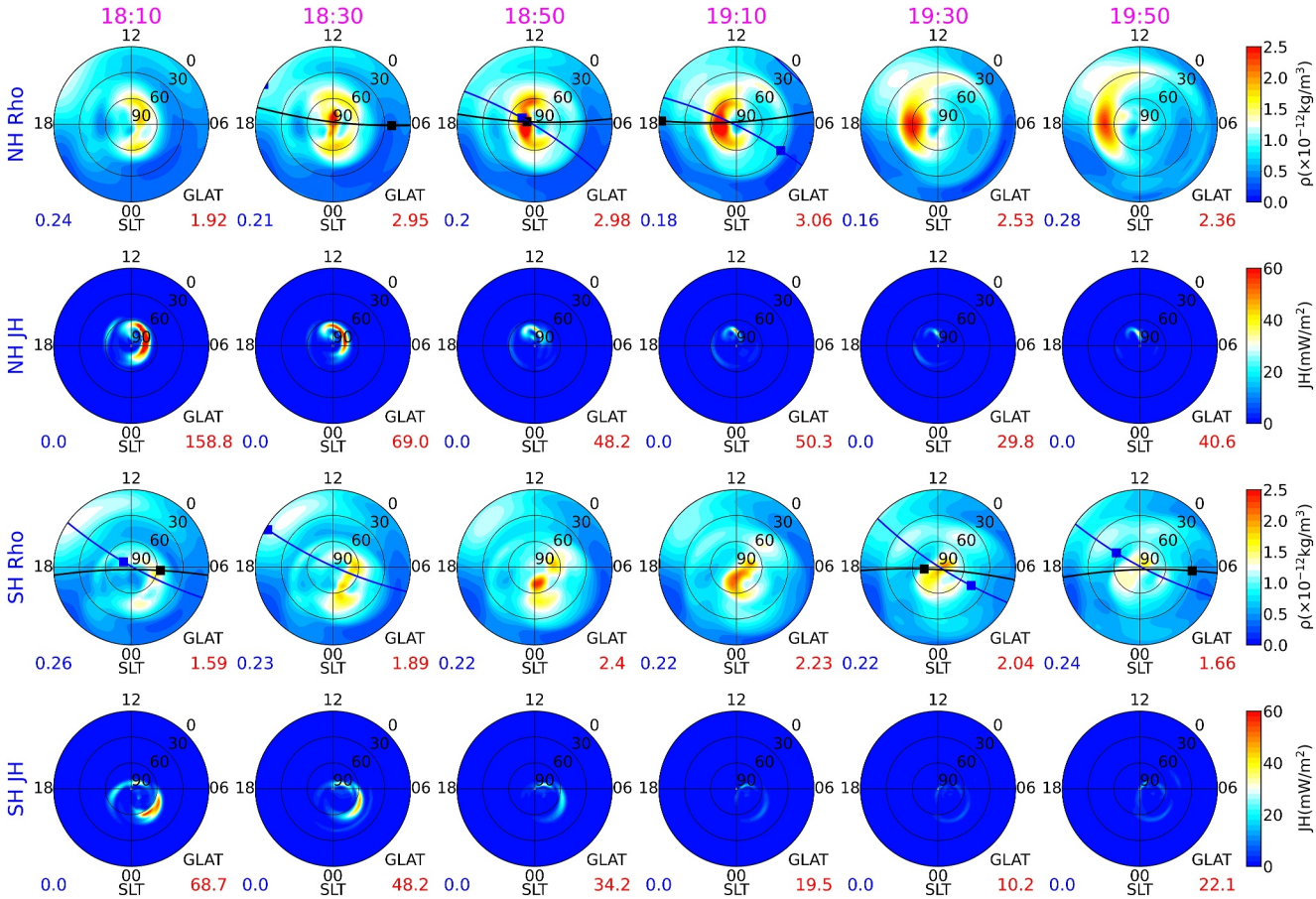

Figure 6. Evolutions of the simulated neutral mass density at 500 km and height-integrated Joule heating from a polar view. The top two panels represent the Northern Hemisphere, while the bottom two panels depict the Southern Hemisphere, covering the time span between 18 and 20 UT on 13 March 2022. Each plot is presented with respect to solar local time and geographic latitude, and the minimum and maximum of the parameter is indicated on the bottom left and bottom right, respectively. Additionally, the first and third panels include markers indicating the locations and lines denoting the trajectories of available satellites (blue: GRACE-FO; black: Swarm-C).

heating on the dawn side is substantially greater in the NH compared to the SH before 18:30 UT, leading to notably larger Joule heating deposited in the NH (Figure 2f). Associated with the regions of strong Joule heating deposition, notable neutral density enhancements occur nearby. Specifically, elongated neutral mass density structures, termed HDAs in this study, can be identified poleward of the dawnside Joule heating deposition region around 18:30 UT in the NH and 18:50 UT in the SH. In the NH, the HDA subsequently propagates to the dusk sides along the 6–18 SLT direction. After 18:30 UT, the HDA moves into the dusk side and is detected by both GRACE-FO and Swarm-C satellites at geographic latitudes between 70° and 80°N around 18:50 UT. Therefore, the neutral density spikes shown in Figure 5b are manifestations of this HDA, which spans an extension of around 6 hr in SLT. However, no significant Joule heating is observed in collocation with this HDA. Additionally, there is no significant Joule heating deposition at 70°–80°N geographic latitudes on the dusk side before the arrival of this HDA. After the detection, this NH HDA continues propagating equatorward on the dusk side, which will be discussed later. The magnitude of the HDA increases after its formation until 19:10 UT and then begins to subside. In the SH, an HDA forms around 18:50 UT at a post-midnight location near 70°S geographic latitude. The HDA exhibits a poleward movement along the 3–15 SLT direction with a decreasing magnitude. Both GRACE-FO and Swarm-C satellites pass over this structure between 19:30 and 19:50 UT. Hence, the neutral density spikes shown in Figure 5c are manifestations of this SH HDA. Between 19:30 and 19:50 UT, this SH HDA is located near the South Pole and aligns with the 9–21 SLT, extending approximately 6,000 km. Similar to its NH counterpart, the SH HDA is not collocated with any significant Joule heating deposition during its propagation. However, the movement of this SH HDA is slower than that of the NH HDA, and its peak magnitude is smaller than that observed in the NH.

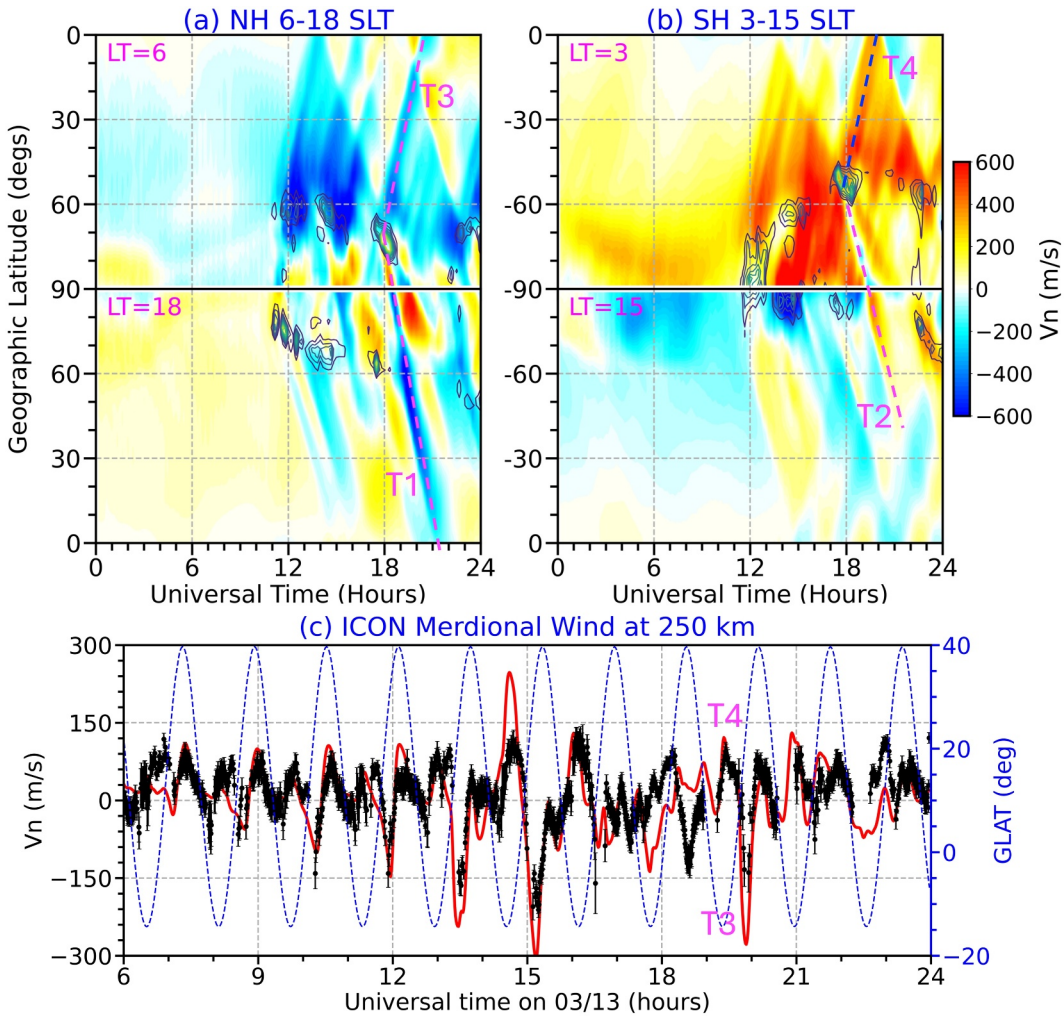

Figure 7. (a) and (b) Simulated meridional wind at an altitude of 500 km in the NH and SH, respectively. Plots a and b show the simulation results along 6–18 SLT and 3–15 SLT, respectively, plotted against universal time and geographic latitude. Positive winds denote northward winds. Several traveling atmospheric disturbances are labeled in plots (a) and (b). Contour lines in plots a and b represent the height-integrated Joule heating. (c) Comparisons between observed and simulated meridional winds at an altitude of 250 km for the ICON-MIGHTI on 13 March 2022. Observational data are shown by dots with error bars, while simulation results are illustrated with red lines. The geographic latitudes of ICON-MIGHTI measurements are indicated by the blue dashed line. The corresponding signals in the observation related to T3 and T4 are highlighted in plot (c).

It is evident from the simulation that the HDAs shown in Figure 6 are not associated with in-situ Joule heating. Given their propagation characteristics, it is plausible that these HDAs are manifestations of transpolar TADs (Bruinsma & Forbes, 2009; Lu et al., 2016). As depicted in Figure 6, the properties of the TADs in the NH and SH may exhibit notable differences. For example, the NH transpolar TAD seems to have a stronger magnitude and the faster phase speeds. To further illustrate the differences in the transpolar TADs in the NH and SH, Figures 7a and 7b show the meridional wind at an altitude of 500 km as a function of Universal Time (UT) and geographic latitude in the NH and SH, respectively. Specifically, Figures 7a and 7b correspond to the 6–18 SLT sector and the 3–15 SLT sector, respectively. Positive winds correspond to northward winds. Upon a closely examination of the neutral mass density and meridional wind outputs, the transpolar TADs associated with the observed HDAs in the NH and SH are identified as T1 and T2, respectively. Specifically, T1 travels with a phase speed of 1,000 m/s, while T2 moves at a slower phase speed of 700 m/s. Additionally, T1 exhibits a relatively stronger magnitude compared to T2. For instance, the equatorward wind associated with T1 at 60°N and 18 SLT reach a speed of 550 m/s, whereas the equatorward wind associated with T2 at 60°S and 15 SLT only reaches a speed of 100 m/s. Notably, while T1 remains easily detectable at lower latitudes, T2 becomes invisible as it moves toward lower latitudes.

10.1029/2024SW004084

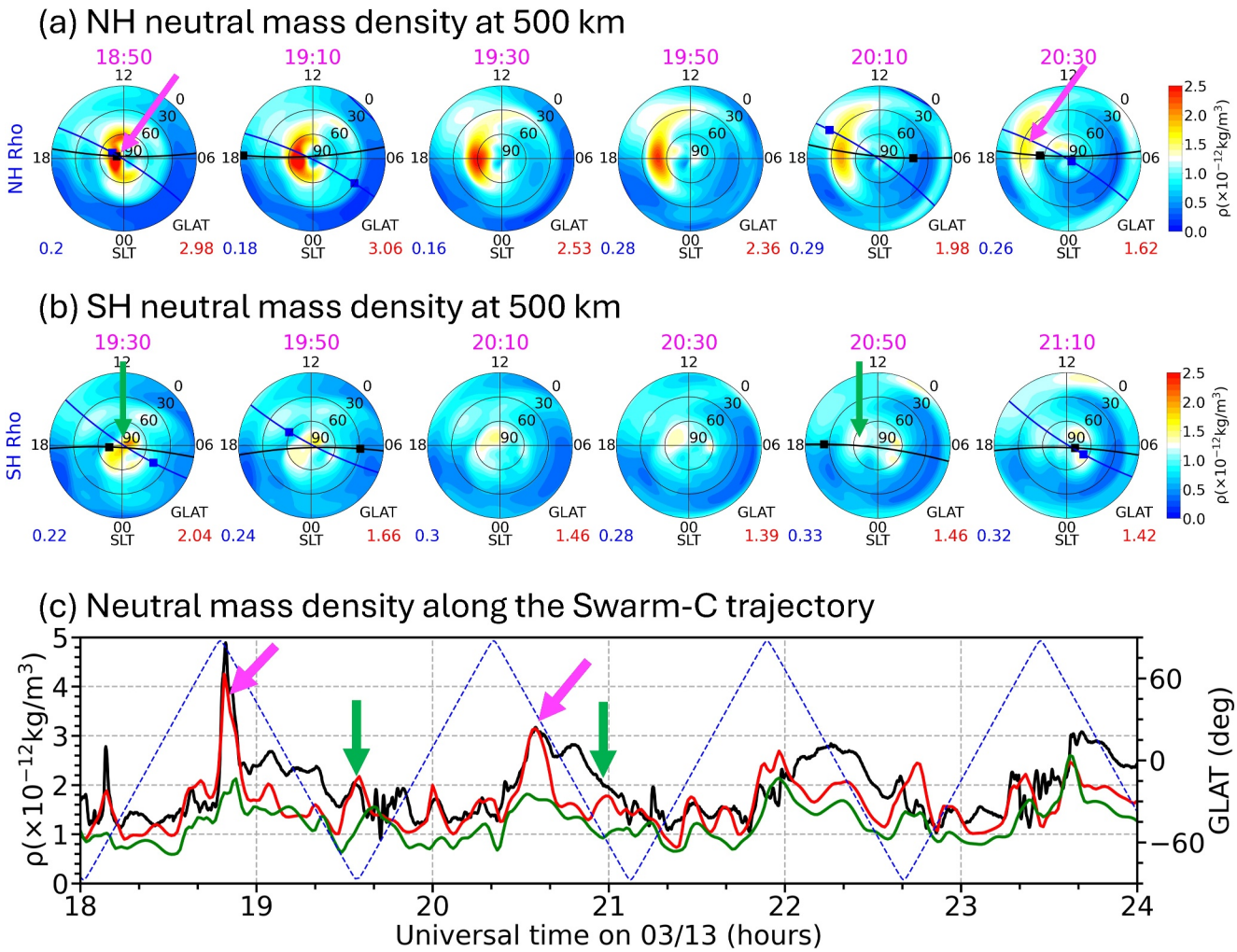

Figure 8. (a) Evolutions of the simulated neutral mass density at 500 km in the Northern Hemisphere (NH) after 18:50 UT on 03/13/2022 from a polar view. (b) Evolutions of the simulated neutral mass density at 500 km in the Southern Hemisphere (SH) after 19:30 UT on 03/13/2022 from a polar view. Each plot in panels a and b are presented with respect to solar local time and geographic latitude, and the minimum and maximum of the parameter is indicated on the bottom left and bottom right, respectively. Additionally, the square indicates the location of the satellite, and the line denotes the trajectory of the satellite (blue: GRACE-FO; black: Swarm-C). (c) Comparisons between observed (black) and simulated (red) thermospheric neutral mass density data for the Swarm-C satellite. The magenta and green arrows represent the spikes from the simulation data in the NH and SH, respectively, and the corresponding spatial structures are highlighted in panels a and b, respectively.

Figure 7c compares the simulated winds with measurements from ICON-MIGHTI at an altitude of 250 km on March 13. GITM generally reproduces the observed meridional wind except for the period between 17:30 and 19:30 UT, confirming its accuracy in capturing the F-region neutral dynamics. The potential cause for the discrepancies observed between 17:30 and 19:30 UT is discussed in the supplementary Text S1 in Supporting Information S1. Notably, GITM captures an intense southward wind spike around 20 UT (marked as T3 in Figure 7c), which corresponds to an equatorward propagating TAD on the dawn side in the NH (Movie S1). The propagation of this TAD at 6 SLT is further highlighted in Figure 7a. Similarly, the northward wind spike before T3 (marked as T4 in Figure 7c) corresponds to an equatorward propagating TAD around midnight in the SH, with its propagation at 3 SLT in the SH also highlighted in Figure 7b. It is noteworthy that T1 and T3 in the NH, and T2 and T4 in the SH, are triggered by the same respective heating sources around 18 UT. Although there are no high-latitude neutral wind measurements available between 18 and 20 UT, the accurate simulation of T3 and T4 by GITM suggests that the simulations of T1 and T2 may also be reliable.

To validate the equatorward propagation of T1 and T2, the evolution of the neutral density after 20 UT is further examined. As shown in Figure 8a, GITM indicates that the Swarm-C satellite passes through the T1 around 20:30 UT near 30°N geographic latitude (Figure 8b). Both Swarm-C and GITM capture the spike associated with this

passage (Figure 8c), suggesting that the equatorward propagation of T1 is realistic. For the T2, GITM suggests that Swarm-C passes through it around 21:00 UT. While GITM shows a moderate spike, Swarm-C does not detect a corresponding spike. This discrepancy could be due to T2 dissipating more quickly than GITM predicts. As shown in Figure 8b, the SH HDA's magnitude decreases over time, indicating that T2 is diminishing, possibly faster than GITM's estimation. Therefore, the equatorward propagation of T2 cannot be confirmed by Swarm-C measurements due to its ~96 min orbital period. A similar conclusion can be drawn from a comparison with GRACE-FO data.

The differences in the propagation direction of the transpolar TADs between the NH and SH can be attributed to the asymmetries in the dawn-side Joule heating distribution between the two hemispheres. As illustrated in Figure 6, the Joule heating is mainly concentrated between 0 and 12 SLT in the NH while it is located between 0 and 6 SLT in the SH. Consequently, the NH TAD follows a path approximately along 6–18 SLT from a polar view, whereas the SH TAD propagates along 3–15 SLT. The differences in the phase speed and magnitude of the transpolar TADs between the NH and SH may stem from the intensity of the Joule heating deposition. As shown in Figure 6, the dawnside Joule heating deposition is significantly stronger in the NH compared to the SH before 18:30 UT, which may further lead to faster and stronger transpolar TADs in the NH (Richmond, 1979). The background thermospheric conditions likely play a significant role as well. For instance, the background thermospheric wind can increase/decrease the phase speed and magnitude of the TAD if the background wind is in the same/opposite directions (Balthazor & Moffett, 1999). As shown in Figures 7a and 7b, prior to the initiation of poleward propagating TADs T1 and T2, the background neutral wind is equatorward, with a much larger speed in the SH. As a result, the poleward propagating TAD in the SH is more strongly modulated by the background neutral wind, leading to a reduced magnitude and slower phase speed compared to the NH TAD. Additionally, due to the offset between the geographic and geomagnetic poles, the geomagnetically high-latitude region in the SH leans toward the nightside, while in the NH it leans toward the dayside (Figure 6). This nightside dominance in the SH results in a relatively lower background neutral density, which could further contribute to a weaker and slower transpolar TAD in the SH compared to the NH. The IHA in the electron precipitation is trivial in GITM (due to the use of ASHLEY-A) so it may not play an important role. The IHA in the ionospheric conductivity (mainly due to the offset of the geomagnetic pole) contribute to the IHA in Joule heating but may not contribute to the IHA in the HDA directly. Hence, the IHAs in the HDA's magnitude and propagation shown in Figure 6 mainly stem from IHAs in Joule heating and background thermospheric condition.

4. Conclusion

In this study, the high-latitude neutral mass density variation during the 13–14 March 2022 storm is investigated, focusing particularly on those related to the second IMF B_z southward turning on March 13. Intense neutral density spikes are detected by GRACE-FO and Swarm-C satellites in both the NH and SH, which are successfully captured by the FAC-driven GITM simulation. GITM simulation indicates those spikes correspond to high-latitude density anomalies (HDAs) formed prior to their detection by the satellites and are manifestations of transpolar TADs triggered by the dawnside Joule heating deposition around 18 UT. GITM simulation further uncovers significant IHAs in the formation and propagation of HDAs. Specifically, the NH HDA originates on the dawn side and propagates along the 6–18 SLT direction with a speed of 1,000 m/s, whereas the SH HDA forms in the post-midnight sector and propagates along the 3–15 SLT direction with a speed of 700 m/s. Additionally, the NH HDA tends to be stronger than the SH HDA. The IHA in the HDA propagation direction can be attributed to the IHAs in the Joule heating distribution. In the NH, Joule heating is primarily concentrated from the dawn to noon side, while in the SH it is mostly from the post-midnight to dawn side. Furthermore, the amount of Joule heating deposited in the NH around 18 UT is significantly greater than that in the SH, which may contribute to the faster and stronger transpolar TAD in the NH and further leads to the faster and stronger NH HDA. In addition, it is found that the IHAs in the background thermospheric wind and neutral density may further lead to the IHAs in HDA's magnitude and propagation. This study provides new insights into the IHAs in the high-latitude neutral mass density variations when the IMF B_y is non-negligible.

Data Availability Statement

The IMF and SYM-H data can be found at https://omniweb.gsfc.nasa.gov. The Swarm-C neutral mass density data is available at https://swarm-diss.eo.esa.int/#swarm%2FLevel2daily%2FEntire_mission_data%2FDNS%

2FACC%2FSat_C and the GRACE-FO neutral mass density data is available at https://swarm-diss.eo.esa.int/#swarm%2FMultimission%2FGRACE-FO%2FDNS%2FSat_1. The ICON-MIGHTI wind data are available at https://icon.ssl.berkeley.edu/Data. The AMPERE FAC data are available at https://ampere.jhuapl.edu/. The DMSP and GITM outputs are available at Zhu (2024).

Acknowledgments
This work conducted at UT Dallas was supported by the NSF Award AGS-2431590. QZ and GL were also supported by the NASA Grant 80NSSC22K0061 through the subaward 2021GC1619. GL was also supported in part by NASA LWS Program under award 80NSSC20K1784 and by NASA HSR Program under award 80NSSC21K1673. This material is based upon work supported by the National Center for Atmospheric Research, which is a major facility sponsored by the National Science Foundation under Cooperative Agreement No. 1852977. This research was supported by the International Space Science Institute (ISSI) in Bern and Beijing, through ISSI International Team project #511 (Multi-Scale Magnetosphere-Ionosphere-Thermosphere Interaction). We would like to acknowledge high-performance computing support from Cheyenne (https://doi.org/10.5065/D6RX99HX) provided by National Center for Atmospheric Research's Computational and Information Systems Laboratory, sponsored by the National Science Foundation.

References

Aa, E., Ridley, A. J., Zhang, D., & Xiao, Z. (2012). Analyzing the hemispheric asymmetry in the thermospheric density response to geomagnetic storms. *Journal of Geophysical Research*, *117*(A8). https://doi.org/10.1029/2011JA017259

Aa, E., Zhang, S., Erickson, P. J., Wang, W., Qian, L., Cai, X., et al. (2023). Significant mid- and low-latitude ionospheric disturbances characterized by dynamic EIA, EPBs, and SED variations during the 13–14 March 2022 geomagnetic storm. *Journal of Geophysical Research: Space Physics*, *128*(8), e2023JA031375. https://doi.org/10.1029/2023JA031375

Anderson, B. J., Angappan, R., Barik, A., Vines, S. K., Stanley, S., Bernasconi, P. N., et al. (2021). Iridium communications satellite constellation data for study of Earth's magnetic field. *Geochemistry, Geophysics, Geosystems*, *22*(8), e2020GC009515. https://doi.org/10.1029/2020GC009515

Balthazor, R. L., & Moffett, R. J. (1999). Morphology of large-scale traveling atmospheric disturbances in the polar thermosphere. *Journal of Geophysical Research*, *104*(A1), 15–24. https://doi.org/10.1029/1998JA900039

Bruinsma, S., Forbes, J. M., Nerem, R. S., & Zhang, X. (2006). Thermosphere density response to the 20–21 November 2003 solar and geomagnetic storm from CHAMP and GRACE accelerometer data. *Journal of Geophysical Research*, *111*(A6). https://doi.org/10.1029/2005JA011284

Bruinsma, S. L., & Forbes, J. M. (2009). Properties of traveling atmospheric disturbances (TADs) inferred from CHAMP accelerometer observations. *Advances in Space Research*, *43*(3), 369–376. https://doi.org/10.1016/j.asr.2008.10.031

Deng, Y., Lin, C. Y., Zhu, Q., & Sheng, C. (2021). Influence of nonhydrostatic processes on the ionosphere-thermosphere. In W. Wang, Y. Zhang, & L. J. Paxton (Eds.), *Geophysical monograph series* (1st ed., pp. 65–78). Wiley. https://doi.org/10.1002/9781119815631.ch4

Englert, C. R., Harlander, J. M., Brown, C. M., Marr, K. D., Miller, I. J., Stump, J. E., et al. (2017). Michelson interferometer for global high-resolution thermospheric imaging (MIGHTI): Instrument design and calibration. *Space Science Reviews*, *212*(1–2), 553–584. https://doi.org/10.1007/s11214-017-0358-4

Englert, C. R., Harlander, J. M., Marr, K. D., Harding, B. J., Makela, J. J., Fae, T., et al. (2023). Michelson interferometer for global high-resolution thermospheric imaging (MIGHTI) on-orbit wind observations: Data analysis and instrument performance. *Space Science Reviews*, *219*(3), 27. https://doi.org/10.1007/s11214-023-00971-1

Harding, B. J., Immel, T. J., Mende, S. B., Wu, Y. J., Maute, A., England, S. L., et al. (2024). Day-to-day variability of the neutral wind dynamo observed by ICON: First results from conjugate observations. *Geophysical Research Letters*, *51*(5), e2023GL107110. https://doi.org/10.1029/2023GL107110

Harding, B. J., Makela, J. J., Englert, C. R., Marr, K. D., Harlander, J. M., England, S. L., & Immel, T. J. (2017). The MIGHTI wind retrieval algorithm: Description and verification. *Space Science Reviews*, *212*(1–2), 585–600. https://doi.org/10.1007/s11214-017-0359-3

Hładczuk, N. A., Van Den Ijssel, J., Kodikara, T., Siemes, C., & Visser, P. (2024). GRACE-FO radiation pressure modelling for accurate density and crosswind retrieval. *Advances in Space Research*, *73*(5), 2355–2373. https://doi.org/10.1016/j.asr.2023.12.059

Hong, Y., Deng, Y., Zhu, Q., Maute, A., Sheng, C., Welling, D., & Lopez, R. (2021). Impacts of different causes on the inter-hemispheric asymmetry of ionosphere-thermosphere system at mid- and high-latitudes: GITM simulations. *Space Weather*, *19*(11), e2021SW002856. https://doi.org/10.1029/2021SW002856

Huang, C. Y., Huang, Y., Su, Y.-J., Huang, T., & Sutton, E. K. (2017). High-latitude neutral mass density maxima. *Journal of Geophysical Research: Space Physics*, *122*(10). https://doi.org/10.1002/2017JA024334

Immel, T. J., England, S. L., Mende, S. B., Heelis, R. A., Englert, C. R., Edelstein, J., et al. (2018). The ionospheric connection explorer mission: Mission goals and design. *Space Science Reviews*, *214*(1), 13. https://doi.org/10.1007/s11214-017-0449-2

Li, M., Deng, Y., Harding, B. J., & England, S. (2024). Climatology of dayside E-region zonal neutral wind shears from ICON-MIGHTI observations. *Space Weather*, *22*(2), e2023SW003670. https://doi.org/10.1029/2023SW003670

Li, R., & Lei, J. (2021). Responses of thermospheric mass densities to the October 2016 and September 2017 geomagnetic storms revealed from multiple satellite observations. *Journal of Geophysical Research: Space Physics*, *126*(1). https://doi.org/10.1029/2020JA028534

Liu, R., Lühr, H., & Ma, S.-Y. (2010). Storm-time related mass density anomalies in the polar cap as observed by CHAMP. *Annales Geophysicae*, *28*(1), 165–180. https://doi.org/10.5194/angeo-28-165-2010

Lu, G., Richmond, A. D., Lühr, H., & Paxton, L. (2016). High-latitude energy input and its impact on the thermosphere. *Journal of Geophysical Research: Space Physics*, *121*(7), 7108–7124. https://doi.org/10.1002/2015JA022294

Makela, J. J., Baughman, M., Navarro, L. A., Harding, B. J., Englert, C. R., Harlander, J. M., et al. (2021). Validation of ICON-MIGHTI thermospheric wind observations: 1. Nighttime red-line ground-based Fabry-Perot interferometers. *Journal of Geophysical Research: Space Physics*, *126*(2), e2020JA028726. https://doi.org/10.1029/2020JA028726

Maute, A., & Richmond, A. D. (2017). F-Region dynamo simulations at low and mid-latitude. *Space Science Reviews*, *206*(1–4), 471–493. https://doi.org/10.1007/s11214-016-0262-3

Oliveira, D. M., & Zesta, E. (2019). Satellite orbital drag during magnetic storms. *Space Weather*, *17*(11), 1510–1533. https://doi.org/10.1029/2019SW002287

Prölss, G. W. (2011). Density perturbations in the upper atmosphere caused by the dissipation of solar wind energy. *Surveys in Geophysics*, *32*(2), 101–195. https://doi.org/10.1007/s10712-010-9104-0

Richmond, A. D. (1979). Thermospheric heating in a magnetic storm: Dynamic transport of energy from high to low latitudes. *Journal of Geophysical Research*, *84*(A9), 5259–5266. https://doi.org/10.1029/JA084iA09p05259

Richmond, A. D. (2021). Joule heating in the thermosphere. In W. Wang, Y. Zhang, & L. J. Paxton (Eds.), *Geophysical monograph series* (1st ed., pp. 1–18). Wiley. https://doi.org/10.1002/9781119815631.ch1

Ridley, A. J., Deng, Y., & Tóth, G. (2006). The global ionosphere–thermosphere model. *Journal of Atmospheric and Solar-Terrestrial Physics*, *68*(8), 839–864. https://doi.org/10.1016/j.jastp.2006.01.008

Sheng, C., Deng, Y., Bristow, W. A., Nishimura, Y., Heelis, R. A., & Gabrielse, C. (2022). Multi-scale geomagnetic forcing derived from high-resolution observations and their impacts on the upper atmosphere. *Space Weather*, *20*(12), e2022SW003273. https://doi.org/10.1029/2022SW003273

Sutton, E. K., Forbes, J. M., & Nerem, R. S. (2005). Global thermospheric neutral density and wind response to the severe 2003 geomagnetic storms from CHAMP accelerometer data. *Journal of Geophysical Research*, *110*(A9). https://doi.org/10.1029/2004JA010985

Tyska, J., Deng, Y., Zhang, S., & Lin, C. Y. (2024). Ionospheric disturbances generated by the 2015 Calbuco eruption: Comparison of GITM-R simulations and GNSS observations. *Space Weather*, *22*(2), e2023SW003502. https://doi.org/10.1029/2023SW003502

Waters, C. L., Anderson, B. J., Green, D. L., Korth, H., Barnes, R. J., & Vanhamäki, H. (2020). Science data products for AMPERE. In M. W. Dunlop & H. Lühr (Eds.), *Ionospheric multi-spacecraft analysis tools: Approaches for deriving ionospheric parameters* (pp. 141–165). Springer International Publishing. https://doi.org/10.1007/978-3-030-26732-2_7

Yamazaki, Y., Kosch, M. J., & Sutton, E. K. (2015). North-South asymmetry of the high-latitude thermospheric density: IMF BY effect. *Geophysical Research Letters*, *42*(2), 225–232. https://doi.org/10.1002/2014GL062748

Zhu, Q. (2024). Data for "Interhemispheric asymmetry in the high-latitude neutral density variations during the 13-14 March 2022 storm [Dataset]. *Zenodo*. https://doi.org/10.5281/zenodo.12734373

Zhu, Q., Deng, Y., Maute, A., Kilcommons, L. M., Knipp, D. J., & Hairston, M. (2021). Ashley: A new empirical model for the high-latitude electron precipitation and electric field. *Space Weather*, *19*(5), e2020SW002671. https://doi.org/10.1029/2020SW002671

Zhu, Q., Lu, G., Lei, J., Deng, Y., Doornbos, E., Van Den Ijssel, J., & Siemes, C. (2023). Interhemispheric asymmetry of the thermospheric neutral density response to the 7–9 September 2017 geomagnetic storms. *Geophysical Research Letters*, *50*(11), e2023GL103208. https://doi.org/10.1029/2023GL103208

Zhu, Q., Lu, G., Maute, A., Deng, Y., & Anderson, B. (2022). Assessment of using field-aligned currents to drive the global ionosphere thermosphere model: A case study for the 2013 St Patrick's day geomagnetic storm. *Space Weather*, *20*(9), e2022SW003170. https://doi.org/10.1029/2022SW003170